Brain Structure and Function
https://doi.org/10.1007/s00429-020-02085-8

ORIGINAL ARTICLE

A systematic comparison of structural-, structural connectivity-, and functional connectivity-based thalamus parcellation techniques

Charles Iglehart[1] · **Martin Monti**[2,3] · **Joshua Cain**[2] · **Thomas Tourdias**[4] · **Manojkumar Saranathan**[1,5]

Received: 9 September 2019 / Accepted: 9 May 2020

Abstract

The thalamus consists of several histologically and functionally distinct nuclei increasingly implicated in brain pathology and important for treatment, motivating the need for development of fast and accurate thalamic parcellation. The contrast between thalamic nuclei as well as between the thalamus and surrounding tissues is poor in T1- and T2-weighted magnetic resonance imaging (MRI), inhibiting efforts to date to segment the thalamus using standard clinical MRI. Automatic parcellation techniques have been developed to leverage thalamic features better captured by advanced MRI methods, including magnetization prepared rapid acquisition gradient echo (MP-RAGE), diffusion tensor imaging (DTI), and resting-state functional MRI (fMRI). Despite operating on fundamentally different image contrasts, these methods claim a high degree of agreement with the Morel stereotactic atlas of the thalamus. However, no comparison has been undertaken to compare the results of these disparate parcellation methods. We have implemented state-of-the-art structural-, diffusion-, and functional imaging-based thalamus parcellation techniques and used them on a single set of subjects. We present the first systematic qualitative and quantitative comparison of these methods. The results show that DTI parcellation agrees more with structural parcellation in the larger thalamic nuclei, while rsfMRI parcellation agrees more with structural parcellation in the smaller nuclei. Structural parcellation is the most accurate in the delineation of small structures such as the habenular, antero-ventral, and medial geniculate nuclei.

Keywords Thalamus nuclei parcellation · MP-RAGE · Diffusion tensor imaging · Resting-state functional MRI

Introduction

The thalamus is a bilateral, subcortical deep brain structure that plays a critical role in numerous neurological processes, including consciousness, memory, and attention. It consists of several histologically distinct nuclei also distinguishable by their global functional implications. The anterior nuclei perform prominent roles in episodic memory (Aggleton 1999) and spatial processing (O'Mara 2013); the mediodorsal (Md) nucleus has been shown to be involved in working memory (Watanabe et al. 2012); the lateral geniculate nucleus (LGN) exhibits a strong functional relationship with the visual cortex (Chen et al. 1998). Recent research has challenged the notion of the thalamus as a passive relay mechanism. For instance, the visual thalamic reticular and mediodorsal nuclei have been shown to dynamically modulate connectivity with the prefrontal cortex (Wimmer et al. 2015; Schmitt et al. 2017). The thalamic nuclei have also been shown to be selectively vulnerable to certain pathological conditions: changes in the limbic nuclei

Electronic supplementary material The online version of this article (https://doi.org/10.1007/s00429-020-02085-8) contains supplementary material, which is available to authorized users.

✉ Charles Iglehart
ciglehart@email.arizona.edu

[1] Department of Electrical and Computer Engineering, University of Arizona, Tucson, AZ, USA

[2] Department of Psychology, University of California Los Angeles, Los Angeles, CA, USA

[3] Neurosurgery Brain Research Center, University of California Los Angeles, Los Angeles, CA, USA

[4] Service de Neuroimagerie Diagnostique Et Thérapeutique and INSERM U1215, Université de Bordeaux, Bordeaux, France

[5] Department of Medical Imaging, University of Arizona, Tucson, AZ, USA

Published online: 21 May 2020

have been associated with the occurrence of Alzheimer's Disease (Braak and Braak 1991); volumetric changes in the Md and pulvinar (Pul) nuclei have been observed in persons afflicted by schizophrenia and schizotypal personality disorder (Andreasen 1997; Byne et al. 2001); degradation of the intralaminar nuclei has been associated with the progression of Parkinson's Disease (Henderson et al. 2000) as well as the depth of the impairment and recovery post severe brain injury (Schiff 2010); multiple nuclei bordering the third ventricle have shown selective vulnerability and atrophy in patients with multiple sclerosis (Planche et al. 2019). Thalamic nuclei have been targeted for treatment of neurological disorders. For example, chronic high-frequency deep brain stimulation of the ventralis intermedius (VIM) nucleus has proven effective in the suppression of essential tremor (Benabid et al. 1991) and has shown the ability to enhance responsiveness in patients with severe disorders of consciousness (Schiff et al. 2007). Until recently, thalamic nuclei could only be distinguished via histology or time-consuming manual parcellation, but a quickly broadening array of noninvasive magnetic resonance imaging (MRI)-based parcellation techniques are showing promise in rapid, and accurate parcellation of thalamic nuclei in vivo.

MRI-based thalamus parcellation techniques developed to date can be broadly grouped into three classes corresponding to three different types of image acquisition-structural imaging, diffusion tensor imaging (DTI), and resting-state functional MRI (fMRI). Structural image contrast arises from the variation of T1 or T2 relaxation parameters between different tissues; DTI uses signal variation corresponding to the diffusion of molecular water as restricted by microstructure; fMRI leverages the differential paramagnetism and diamagnetism of deoxyhemoglobin and oxyhemoglobin (respectively) to measure a blood oxygen level-dependent (BOLD) T2*-weighted signal which is an indirect measure of function. In general, variation of one of these features in the thalamic nuclei need not necessarily correspond with the variation of any of the others. For instance, a region exhibiting a distinctive BOLD signal may be indistinguishable from surrounding tissues from the perspective of a structural acquisition. Thus, parcellation techniques based on differing acquisition types can be expected to produce different results.

Several parcellation methods based on structural MRI have been developed. Approaches using T1- and T2-weighted images were some of the first to be implemented (Deoni et al. 2005; Traynor et al. 2011), but these methods are inhibited by poor contrast between the intrathalamic nuclei as well as between the thalamus and surrounding tissues. Sudyadhom et al. (2009) developed a Fast Gray Matter Acquisition T1 Inversion Recovery (FGATIR) sequence for more reliably visualizing subcortical structures like the ventral intermediate nucleus for deep brain stimulation targets. This sequence did allow for the localization of the entire thalamus but was not optimized to provide the intrathalamic contrast required for structural parcellation. Most recent structural imaging methods involve the use of Magnetization Prepared Rapid Acquisition Gradient Echo (MP-RAGE) or its variants. The method developed by Iglesias et al (2018) applied Bayesian methods to a probabilistic thalamus atlas derived from both ex-vivo histology and in-vivo MP-RAGE to segment the thalamus and was made publicly available as part of the Freesurfer processing platform. A recently developed technique called Thalamus Optimized Multi-Atlas Segmentation ('THOMAS' Su et al. 2019) uses White-matter-nulled (WMn) MP-RAGE (Saranathan et al. 2015) images to drive a multi-atlas parcellation technique that has shown excellent agreement with manual parcellations guided by the Morel stereotactic anatomical atlas (Morel 1997).

The majority of methods published to date are diffusion-MRI-based techniques. DTI can be used to examine microstructure both globally (e.g., through tractography and cortical connectivity analysis) and locally [via tensor analysis and scalar maps, including but not limited to fractional anisotropy (FA), mean apparent propagator (MAP), mean diffusivity (MD), etc]. Parcellation techniques based on global connectivity such as the tractography-based estimates of the cortical projections of particular thalamic nuclei (Behrens et al. 2003; Yamada et al. 2010; Jbabdi et al. 2009) have shown to be reliable. However, they require manual delineation of the relevant cortical regions by an experienced neuroradiologist, which is time consuming. While these methods have demonstrated accuracy in identifying particular nuclear groups (i.e., the ventral nuclei), they have not appeared to reliably identify smaller nuclei. Locally, DTI can be leveraged in a variety of ways to provide voxel-level models of diffusion behavior. These models vary greatly in complexity and must be used judiciously to properly represent the structure of interest. Fitting second-order tensors to the measured diffusion data assigns an ellipsoid to each voxel whose orientation and eccentricity correspond to the primary direction of diffusion and anisotropy, respectively (Basser et al. 1994). Clustering via dominant diffusion orientation (obtained via eigendecomposition of the diffusion tensors) has been used extensively to identify subregions of the thalamus (Unrath et al. 2008; Mang et al. 2012; Kumar et al. 2015). Such methods are fast and simple to implement but can produce spatially disconnected regions owing to the fact that the clustering as implemented accounts exclusively for directional (and not spatial) proximity. Techniques incorporating measures of both spatial and tensorial similarity have been developed (Wiegell et al. 2003; Rittner et al. 2010), but the use of tensors as a diffusion model is ultimately and inherently limited by its inability to represent complex

small-scale fiber tract geometries such as intra-voxel bending, crossing, and twisting (Basser et al. 2000). Recent years have seen progressive refinement in the modeling used to represent small-scale diffusion architecture. Q-Ball Imaging (QBI) (Tuch 2004) utilizes model-independent spherical tomographic reconstruction to produce white matter fiber orientation distributions (FODs) capable of resolving fiber crossing. As more DTI directions are collected, at the expense of longer scan time, higher order QBI parametrizations can be performed, and finer scale structures can be modeled. The most consistent DTI-based parcellation developed to date uses QBI-derived FOD parameters interior to the thalamus to identify specific nuclei (Battistella et al. 2017). In general, DTI's reliance on echo-planar imaging (EPI) results in lower resolution images relative to other acquisition types, typically on the order of 2–3 mm^3. In addition, the predominance of gray matter in the thalamus dictates a largely isotropic diffusion profile which has inhibited the performance of DTI-based parcellation techniques.

Analysis of resting-state functional MRI (fMRI) has been used to explore functional relationships between cortical regions of interest (ROIs) and individual thalamic nuclei (Kumar et al 2017). Zhang et al. (2008) proposed one of the first fMRI thalamic parcellation algorithms by correlating each thalamic voxel against a set of cortical ROIs delineated by their distinct functional roles. This study showed that each thalamus voxel correlated strongly with only one region, suggesting strong resting-state functional specialization. Ji et al (2016) built upon this by using several temporally independent thalamocortical states with generally closer correlation with the Morel atlas, but this method required a large number of subjects and intensive processing. The method proposed in van Oort et al. (2018) extends the use of fMRI for parcellation of cortical and subcortical structures including the thalamus. This technique leverages instantaneous temporal correlations in the BOLD signal to identify functionally distinct subregions within a ROI. Instantaneous connectivity parcellation (ICP) techniques are used to partition the thalamus via subspace projection. This method also employs a data-driven technique for identifying an optimal number of segments for the final parcellation.

Methods using each image acquisition class claim high measures of agreement with the same anatomical atlases (typically the Morel atlas), yet the underlying acquisition types measure fundamentally different features. This suggests that an examination is warranted to determine how parcellation methods predicated on differing acquisition classes compare and contrast both qualitatively and quantitatively. Furthermore, such a comparison might facilitate multimodal parcellation, if the techniques provided similar and/or complementary information. Towards that end, this study presents the first systematic comparison of structural-, structural connectivity-, and functional connectivity-based thalamus parcellation techniques run on the same set of subjects.

Methods

MRI acquisition

Multiple image types were collected for 18 healthy individuals who provided prior informed consent following the UCLA IRB-approved procedures. All images were obtained using the Siemens 3 T MAGNETOM Prisma fit MRI machine (Erlangen, Germany) housed at the Staglin Center for Cognitive Neuroscience at UCLA. Pulse sequence parameters for the different sequences are as follows: T1-weighted MP-RAGE: 192 sagittal slices, TR/TE 2000/2.52 ms, 12° flip angle, 1 mm isovoxel resolution, FoV 256 mm, generalized autocalibrating partially parallel acquisitions ["GRAPPA," Griswold (2002)] acceleration factor two; White-matter nulled (WMn) MP-RAGE: 160 axial slices, TR/TE 4000/3.75 ms, inversion time 500 ms, 7° flip angle, 1 mm isovoxel resolution, FoV 256 mm, with GRAPPA acceleration factor two; resting-state BOLD EPI: 54 axial slices, TR/TE 700/33 ms, 70° flip angle, 2.5 mm isovoxel, using a simultaneous multislice ["SMS" Barth (2016)] acquisition with acceleration factor six, for a total of 860 volumes; DTI: 50 axial slices, 64 directions, with three *b*-values of zero and one 1000 s/m^2, TR/TE 7000/93 ms, with 2.0 mm isovoxel resolution, FoV 190 mm.

After a careful review of the literature, three recently developed and promising algorithms for structural-, DTI-, and fMRI-based parcellation were chosen for implementation. THOMAS (Su et al. 2019) was selected for structural parcellation; a FOD-driven method (Battistella et al. 2017) was used for DTI-based parcellation; rsfMRI parcellation was performed via ICP (van Oort et al. 2018). These methods were chosen for their consistency and reproducibility. All methods were implemented in the native individual space to minimize the influence of registration effects upon results. The techniques used are briefly described below.

Structural parcellation method

Structural parcellation was performed via THOMAS (Su et al. 2019), which uses nonlinear image registration and multi-atlas label fusion to achieve thalamic parcellation as depicted in Fig. 1. A multi-atlas prior data set was constructed using a set of 20 WMn volumes manually parcellated by a trained neuroradiologist into distinct nuclei using the Morel stereotactic atlas as a guide. A high SNR 1 mm isotropic WMn-MP-RAGE template was generated by nonlinear registration and averaging of the 20 prior WMn

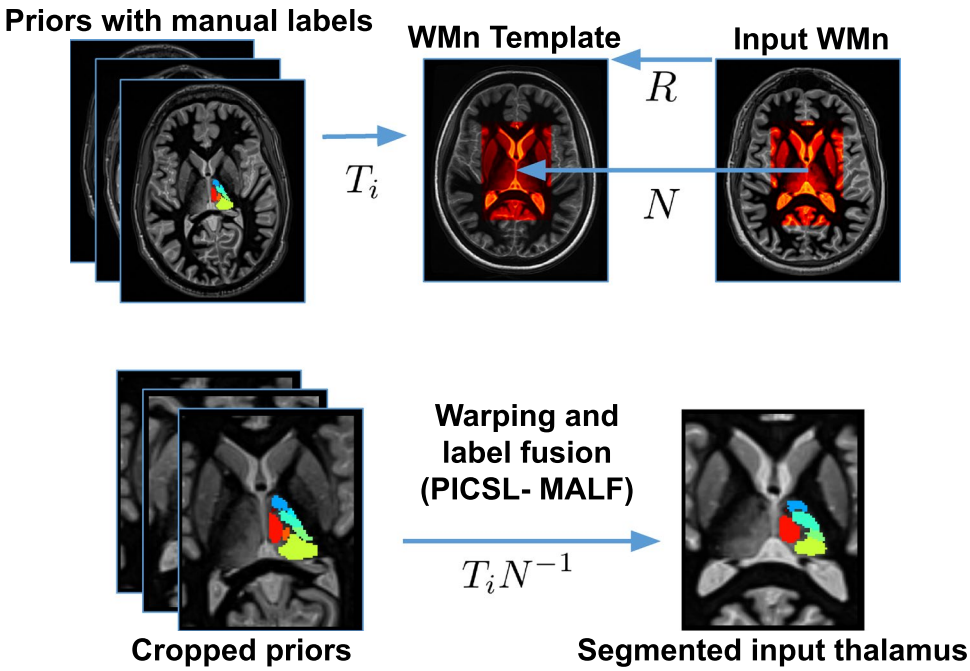

Fig. 1 Structural MRI-based parcellation method (THOMAS). (1) Manually parcellated prior volumes are nonlinearly registered to a template volume with the resulting transformations stored for future use; (2) the entire input volume is rigidly registered to the template; (3) a cropped region of the input surrounding the thalamus is nonlinearly warped to the template; (4) the prior thalamic labels are warped first to the template space and then to the individual input space; (5) the parcellated input thalamus is obtained via label fusion of the warped priors

volumes. To perform thalamic parcellation on an individual input WMn image, the input was first nonlinearly registered to the WMn template. By concatenating the input-to-template warp with WMn priors-to-template warps (which are pre-computed), thalamic nuclei labels from each manually parcellated prior were warped to the input space. The input and template images were automatically cropped to encompass both thalami to speed up the registration process. The final parcellation labels were determined via a joint label fusion process (PICSL-MALF, Wang and Yushkevich 2013), wherein each prior label's contribution to the final parcellation is weighted by the WMn prior's similarity to the input WMn.

DTI parcellation method

DTI parcellation was performed in accordance with the technique described in (Battistella et al. 2017). This method attempts to leverage local diffusion characteristics within the thalamus to inform the parcellation process. Figure 2 gives an overview of the algorithm architecture. DWI denoising, eddy current, and EPI distortion corrections were run using Mrtrix 3.0 'dwidenoise' and 'dwipreproc' utilities. All image registration and transformation was performed via Advanced Normalization Tools [ANTs, ("ANTs by Stnava" n.d. 2019)]. Image parcellation code was written in both Python (Python Software Foundation, https://www.python.org/) and Matlab (The MathWorks, Inc., Natick, Massachusetts, United States). FODs were computed from the input DTI at each voxel within the thalamic mask via the FSL 'qboot' utility, which implements the Q-Ball Imaging algorithm ('QBI,' Tuch 2004). QBI was run with an order six spherical harmonic basis to determine 28 FOD coefficients per voxel. K-means clustering with a modified distance metric incorporating both Euclidean voxel and spherical harmonic (SH) coefficient proximity produced the final parcellation. To ensure that voxel and SH distances contributed equally to the metric, SH coefficients were scaled by a factor of 55 [a scalar determined empirically by Battistella et al. (2017)]. To account for k-means' sensitivity to initial seeding, the centroids of the labels resulting from 5000 k-means runs were used to seed the final parcellation. K-means also requires the number of output clusters be specified in advance of the analysis. A parcellation size of seven clusters has been used extensively in diffusion-based parcellation schema (Battistella et al 2017; O'Muircheartaigh et al. 2011; Behrens 2003) and thus was chosen for this study.

Resting-state fMRI parcellation method

Resting-state fMRI parcellation was performed using Instantaneous Connectivity Parcellation (ICP; van Oort et al. 2018; Kumar et al. 2017). Figure 3 summarizes the algorithm. Prior to applying this method, resting-state blood oxygenation level-dependent (BOLD) data were first preprocessed using FSL (Smith et al. 2004) to remove four initial volumes, apply slice time correction to account for the sequential (bottom-up) acquisition of 2D slices at each volume, perform rigid-body realignment to account for between-volume motion, and spatially smoothed with a Gaussian kernel of 3.5 mm FWHM. It was then temporally smoothed with a high-pass filter of 0.01 Hz only, since

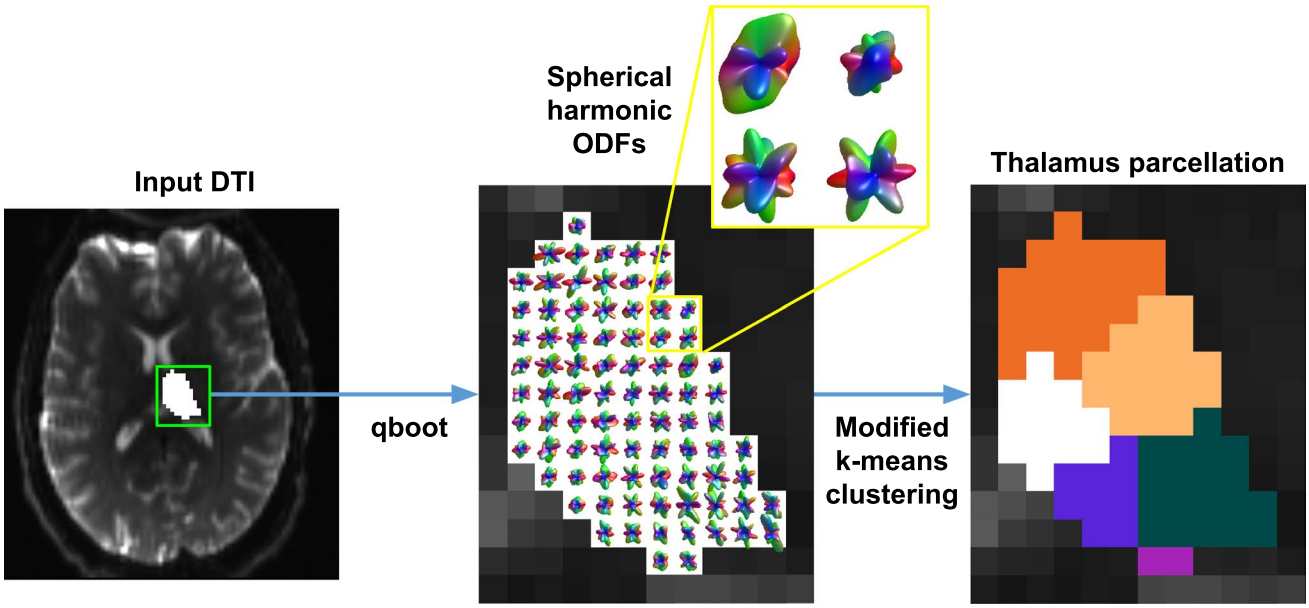

Fig. 2 DTI-based parcellation method. (1) The thalamic mask isolates thalamus voxels within the DTI; (2) order six (28 coefficient) FODs are generated at each voxel in the mask; (3) Modified k-means clustering is run on a linear combination of voxel location values and the FOD coefficients to obtain spatially contiguous labels reflective of local diffusion behavior

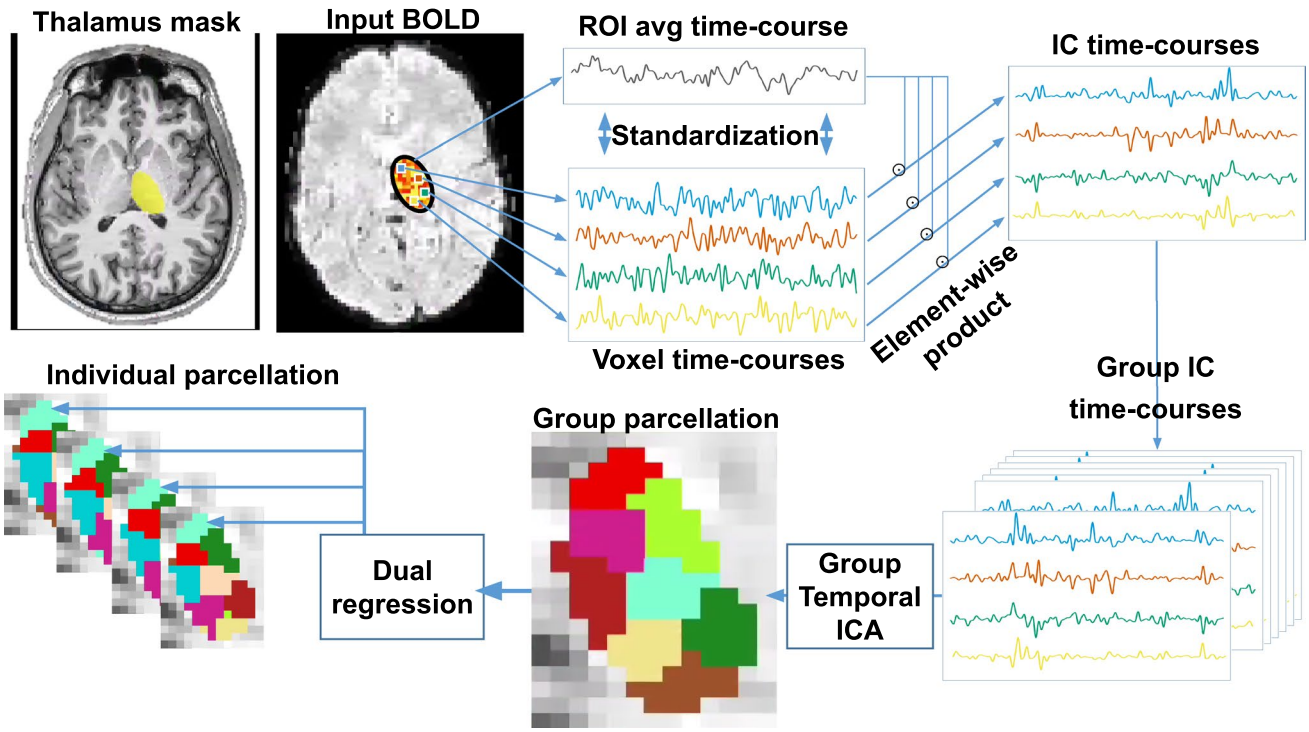

Fig. 3 Schematic of the BOLD rsfMRI processing [as described in van Oort et al. 2018]. (1) Individual thalamic mask is created via single-subject parcellation of the T1-weighted MP-RAGE data; (2) the average time-course across all voxels of thalamus (for each subject and hemisphere separately) is extracted and standardized; (3) each individual voxel's time-course is also extracted, standardized, and then multiplied, element-wise, with the average standardized time-course; (4) these time-courses of instantaneous correlations from all subjects are entered into a group temporal ICA with a set solution dimensionality of 30 components; (5) the resulting group parcellation is then employed to obtain, via dual regression, single-subject parcellation

prior work has shown that resting-state information can be found at much higher frequencies than can be observed when a conventional 0.1 Hz low-pass filter is also used (Wu et al. 2008; Lee et al. 2013). Finally, motion-related artifacts were minimized using the aCompCor50 procedure with 24 motion parameters (Muschelli et al. 2014) and with additional regressors coding for individual high-motion volumes [i.e., 'spike regression'; (Satterthwaite et al. 2013)] as defined by the root mean square difference between a volume and the mid-point volume reference exceeding the outlier threshold of the 75th percentile plus 1.5 times the inter-quartile range (as implemented in fsl_motion_outliers). The residuals forming this nuisance regression were then submitted to the ICP pipeline, which was implemented with an in-house tcsh script combining tools from FSL, Matlab, and AFNI. Following the procedure described by van Oort et al. the ICP was implemented in the following steps applied to each subject and hemisphere separately (see Fig. 3): (1) a thalamic "initialization mask" was created by segmenting the individual T1-weighted MP-RAGE data using FSL FIRST (Patenaude et al. 2011), as implemented in the fsl_anat (https://fsl.fmrib.ox.ac.uk/fsl/fslwiki/fsl_anat) pipeline, and projected into BOLD space; (2) the average time-course of all voxels within the initialization mask (for each hemisphere separately) was extracted and standardized; (3) the time-series of each voxel within the initialization mask were also standardized (individually); (4) the standardized vector obtained in (2) and the standardized voxel time-series obtained in (3) were then multiplied element-wise, for each voxel separately, thereby creating the "unfolded" time-series of instantaneous correlations (cf., van Oort et al. 2018) which were then transformed into MNI template space with a 12 degrees of freedom affine transformation [using FSL FLIRT (Jenkinson and Smith 2001)]. These "unfolded" time-series differ from the original voxel time-series in that they amplify transient events between related time-courses, thereby helping to identify instantaneous correlations between voxels (van Oort et al. 2018). Finally, (5) the unfolded time-series were entered into a group ICA analysis using a temporal concatenation model [as implemented in MELODIC; (Beckmann and Smith 2004)] in order to detect components with coherent spatial topography across individuals (but without requiring them to have similar time-courses across individuals). In order to align the parcellation output across methods, the group ICA enforced a desired solution dimensionality of 30 components, which has been shown in a large cross-validation study to yield the most reproducible results [van Oort et al. 2018]. In addition, a dual regression (Beckman et al. 2009; Nickerson et al. 2017) approach was employed in order to obtain single-subject thalamic ICPs. Specifically, for each subject, the group-average set of parcellation were regressed (as spatial regressors in a multiple regression) into each subject's time-series of instantaneous correlations, thereby generating one subject-specific time-series per group-level parcel. Next, these time-series were regressed (as temporal regressors) into the same 4D dataset, resulting in a set of subject-specific spatial maps, one per group-level spatial map.

Post processing and analysis

Manually delineated ground truth parcellations were not available for this study. Instead, the structural THOMAS outputs were used as gold standard parcellations. THOMAS parcellations have been rigorously validated against manual parcellations guided by the Morel Atlas (Su et al 2019). The use of a multi-atlas (i.e., multiple priors) in THOMAS also makes it preferable to the single-atlas Krauth atlas (Krauth et al 2010), which is based on the average of Morel atlas subjects. All parcellations and volumetry were performed in the native individual space to minimize registration errors. Parcel volumes were computed by determining the number of voxels within each label and multiplying by the method specific individual voxel volume. Dice scores were used to quantitatively compare results between methods. For two cluster labels L_1 and L_2, Dice is defined:

$$\mathrm{Dice}(L_1, L_2) = 2\frac{\|L_1 \cap L_2\|}{\|L_1\| + \|L_2\|},$$

where $\|\bullet\|$ measures the number of voxels in a label, the intersection operation $L_1 \cap L_2$ gives the set of voxels common to both L_1 and L_2, and $|\bullet|$ is the absolute value operation. Individual Dice was averaged to obtain group-level statistical characterizations. Paired sample t tests were used to compare Dice scores between methods with $p = 0.05$ set as significance threshold.

After individual Dice was computed, parcellations were registered and warped (using nearest neighbor interpolation) to the WMn template space for the purpose of group-level analysis. Probability maps were generated for each parcellation technique. Viewed in this common space, these maps can provide insight into average, group-level parcellation characteristics (Najdenovska et al. 2018). Both weighted and maximum probability maps were created. Weighted probability maps were generated by assigning a color to each thalamus voxel representative of the relative proportions of labels present in that voxel across all individual parcellations in the common space. Maximum probability maps were generated by determining the most frequently occurring label in each voxel across all individual parcellations. For both maps, the alpha (transparency) channel of each voxel was weighted by the total number of labels (present across all cases) present in that voxel. These maps can be used as a means of evaluating the spatial consistency of a parcellation in common

space. Diffuse transitions between regions on the map can be indicative of spatial inconsistencies. Maximum probability mapping assigned colors corresponding to the label most commonly present within each voxel.

In addition to using probability maps to gauge consistency, label centroid maps were also created. For each technique, the spatial centroid of each individual label in WMn template space was computed. Centroids for all individuals were overlaid on images of the thalamic region in all three planes. Each centroid label was assigned a label specific color code. Spatial clustering of the label centroids provides a means of evaluating each method for consistency—a tighter clustering of centroids for a particular label in template space is indicative of higher spatial consistency.

Table 1 Index of abbreviations for 11 thalamic nuclei

Nucleus	Abbreviation
Anterior ventral	AV
Centromedian	CM
Habenular	Hb
Lateral geniculate	LGN
Medial geniculate	MGN
Mediodorsal	Md
Pulvinar	Pul
Ventral anterior	VA
Ventral posterolateral	VLp
Ventral lateral anterior	VLa
Ventral posterior lateral	VPl

Results

The three methods were used to parcellate the right and left thalamus for 18 subjects. Table 1 lists abbreviations for eleven thalamic nuclei of interest following the convention in Morel et al. (1997).

Supplemental Table 1a–c provides mean and standard deviation of cluster volumes for all structural-, DTI-, and rsfMRI-based techniques, respectively. The structural parcellations exhibited mean cluster volumes ranging from 34.83 to 1643.56 mm^3 in the left half of the thalamus and from 33.11 to 1621.94 mm^3 in the right; the DTI clusters ranged from 671.56 to 956.56 mm^3 in the left and from 611.22 to 956.94 mm^3 in the right; the rsfMRI clusters ranged from 146.18 to 232.41 mm^3 in the left and from 155.82 to 241.35 mm^3 in the right.

Table 2 compares Dice scores between THOMAS and DTI-based (bold) and THOMAS and rsfMRI-based parcellations separately for the left and right thalamic nuclei. Rows are arranged in descending order of mean structural nucleus volume (listed in the leftmost column). DTI parcellation achieved a maximum Dice of 0.60/0.57 (left/right) in the Md; rsfMRI Dice was highest in the VA (0.38 in the left) and CM (0.38 in the right). In general, DTI exhibited higher Dice values in the larger nuclei, scoring statistically higher (as determined by paired sample t tests, $n = 18$, $p < 0.05$) in both halves of the Pul, VL, Md, and VA; rsfMRI Dice ranked statistically higher several smaller nuclei: the right AV, both halves of the CM, the left MGN and VLa, and both halves of the Hb. Dice scores between DTI and rsfMRI parcellations are reported in supplemental Table 2.

Figure 4 shows axial and sagittal views of left thalamus parcellations for all three methods for two subjects in individual space (WMn-MP-RAGE for structural, $b = 0$

Table 2 Mean and standard deviation of Dice scores between structural- and DTI-based parcellations (bold) and between structural and rsfMRI (italics) for 18 subjects

Structural nucleus (left/right vol, mm^3)	DTI Dice (L)	rsfMRI Dice (L)	DTI Dice (R)	rsfMRI Dice (R)
Pul (1643.56,1621.94)	**0.50 ± 0.06***	*0.21 ± 0.04*	**0.48 ± 0.06***	*0.22 ± 0.05*
VLp (900.28, 911.22)	**0.48 ± 0.06***	*0.30 ± 0.05*	**0.46 ± 0.08***	*0.30 ± 0.05*
Md (714.50, 703.39)	**0.60 ± 0.06***	*0.35 ± 0.08*	**0.57 ± 0.09***	*0.36 ± 0.08*
VA (332.61, 339.83)	**0.44 ± 0.05***	*0.38 ± 0.08*	**0.42 ± 0.05***	*0.34 ± 0.08*
VPL (296.33, 289.72)	**0.33 ± 0.08**	*0.36 ± 0.09*	**0.38 ± 0.06**	*0.35 ± 0.10*
AV (165.22, 167.94)	**0.14 ± 0.03**	*0.13 ± 0.07*	**0.15 ± 0.04**	*0.27 ± 0.09**
CM (122.61, 121.11)	**0.17 ± 0.02**	*0.35 ± 0.11**	**0.14 ± 0.03**	*0.37 ± 0.10**
MGN (85.11, 81.83)	**0.13 ± 0.04**	*0.18 ± 0.10**	**0.12 ± 0.04**	*0.12 ± 0.10*
VLa (74.39, 71.22)	**0.12 ± 0.04**	*0.25 ± 0.16**	**0.10 ± 0.04**	*0.15 ± 0.12*
Hb (34.83, 33.11)	**0.03 ± 0.01**	*0.08 ± 0.06**	**0.03 ± 0.01**	*0.06 ± 0.05**

Nuclei are arranged in descending order of average structural label volume. Mean left and right structural nucleus volumes are given next to the nucleus names in the leftmost column

Statistically significant ($p < 0.05$) differences between methods as measured by two-tailed paired sample t tests are indicated by*

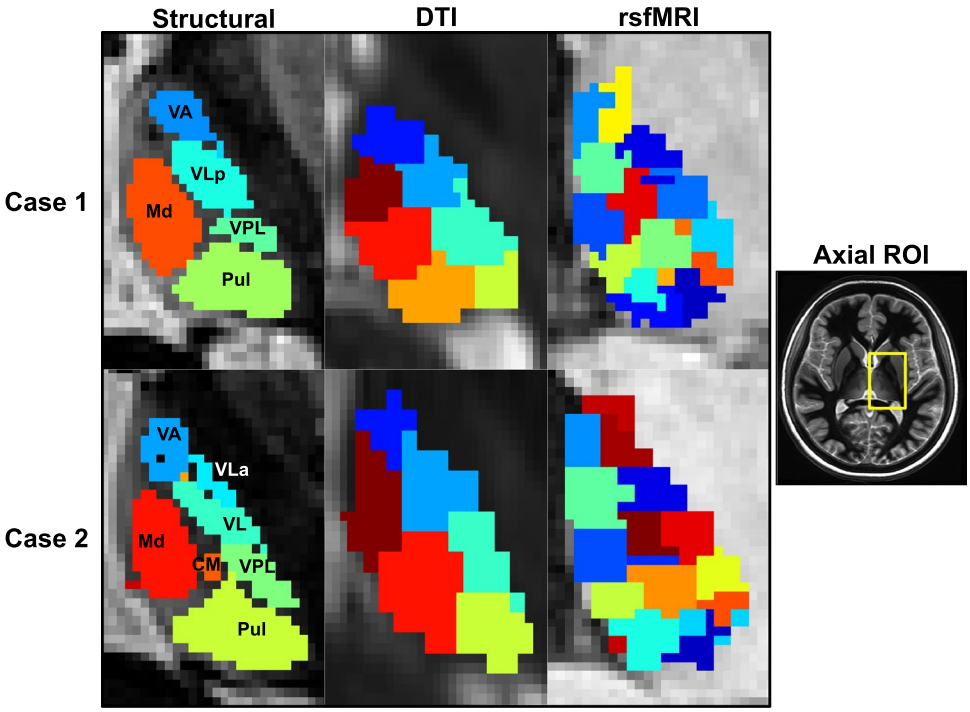

Fig. 4 Axial view of individual thalamic parcellation for two individuals (cases 1 and 2) via structural-, DTI-, and fMRI-based parcellation

for DTI, and T1-weighted for rsfMRI). Parcellations were interpolated to 1 mm^3 isotropic resolution via nearest neighbor interpolation for the purposes of pictorial uniformity. The structural parcellations are labeled for anatomical reference.

Maximum probability maps are shown for axial and sagittal planes in Fig. 5. The maps are depicted in the WMn template space for ease of comparison. The structural maps are the least blurred, suggesting the highest consistency across subjects. The consistency patterns for each method are

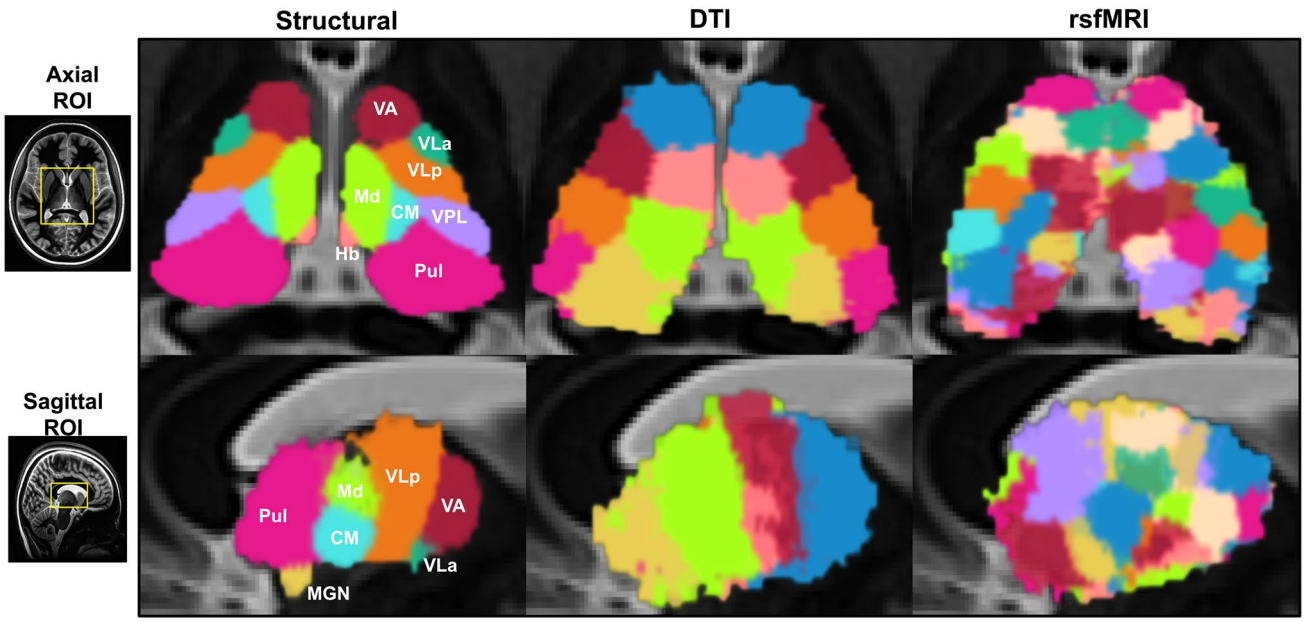

Fig. 5 Axial and sagittal views of maximum probability maps for structural-, DTI-, and rsfMRI-based parcellation. The maps were created by warping individual parcellations to the common WMn template space and identifying the label most commonly present in each voxel. The alpha channel of each voxel is weighted according to the total number of labels occupying that voxel. The maps offer insight into the aggregate behavior of each parcellation method

corroborated by the centroid plots in Fig. 6, where each label centroid is shown projected into the same planes depicted in Fig. 5. The structural centroids cluster more tightly in template space in comparison with those of the DTI and rsfMRI parcellations, suggesting a higher degree of spatial consistency.

Discussion

Reliable and automatic thalamic nuclei parcellation is of considerable interest across a broad array of clinical and research applications. While many parcellation techniques have been proposed, each claiming concordance with the Morel atlas, there exists insufficient analysis of the relative merits of these methods, which are critically tied to acquisition methods. Towards this end, we implemented and compared structural-, diffusion tensor-, and resting-state functional MRI-based thalamic nuclei parcellation methods on a single set of 18 subjects.

We found that DTI- and rsfMRI-based parcellations show complementary correspondence patterns with structural parcellation. On the basis of Dice scores, DTI parcellation more reliably identifies larger nuclei (Pul, VLp, Md, and VA), while rsfMRI shows closer correspondence in the smaller nuclei (CM, AV). Structural parcellation (THOMAS) uses the highest resolution images (1 mm isotropic) and is the only method of the three that reliably identifies smaller nuclei such as Hb, MGN, and VLa.

The number of clusters used by each method is a key design parameter and worthy of further investigation. The rsfMRI method uses split-half reproducibility to settle upon 30 clusters. While this data-driven methodology to choose the number of parcellation nuclei is preferable to a more arbitrary user-supplied parameter (like in the case of DTI-based parcellation), it is unclear whether the 30 subdivisions generated are representative of the actual functional architecture of the thalamus. THOMAS was designed to produce 13 nuclei in correspondence with the Morel atlas (11 of which were selected for analysis in this study). THOMAS was not designed to resolve subdivisions of the Md (Mdm and Mdl) or Pul (PulA and PulM), rather identifying single Md and Pul regions. Supplemental Figure 1 shows maximum probability maps for a prospective regrouping (performed on each individual parcellation) of the 30 rsfMRI clusters into 11 larger clusters compared against structural parcellation. Individual regroupings were performed on the basis of calculated overlap between labels from the rsfMRI and THOMAS maximum probability maps. The regrouped maps suggest that rsfMRI parcellation may consistently

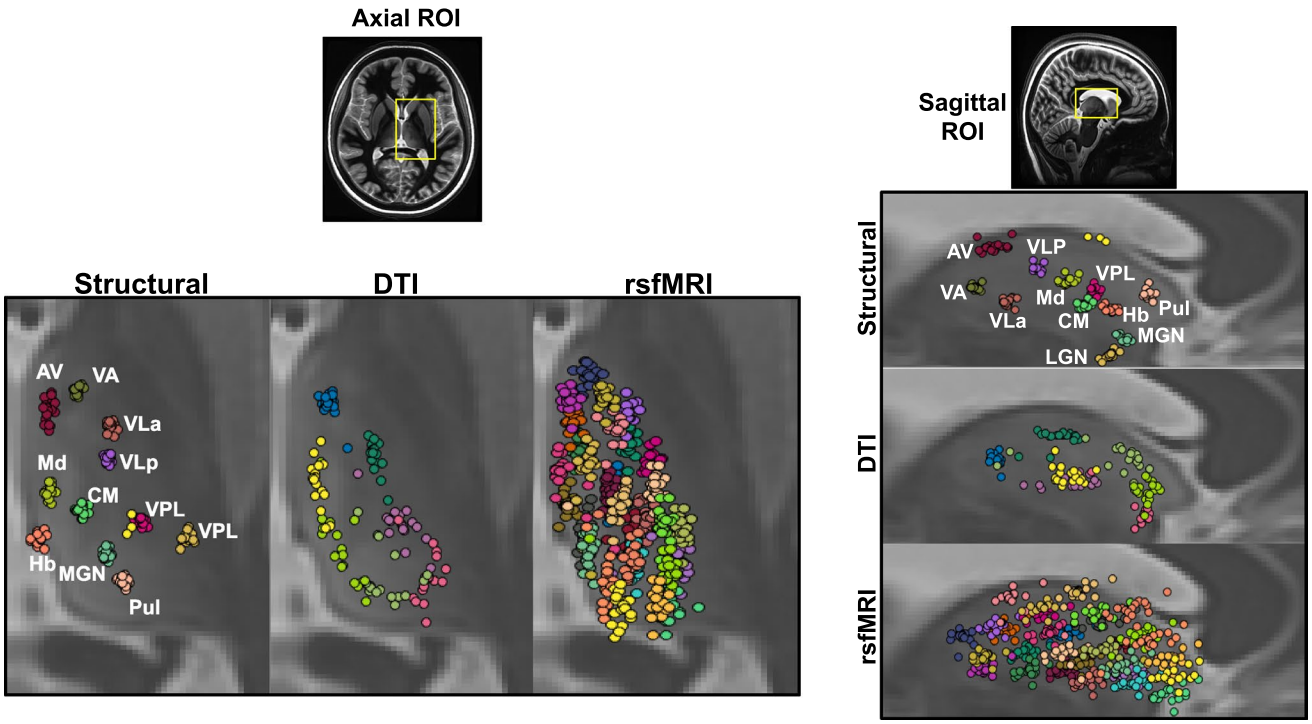

Fig. 6 Axial and sagittal views of label centroid plots for structural-, DTI-, and rsfMRI-based parcellation methods. After individual parcellations were warped to the common WMn template space, the spatial centroid of each parcellation label was computed and plotted with a unique color. Density of centroids for a given label in template space is indicative of the spatial consistency of the corresponding parcellation

identify subdivisions of larger structural nuclei (particularly the Md and Pul). However, the fact that THOMAS maps were required to generate the 11 rsfMRI clusters makes it suboptimal and less of an independent stand-alone method. Supplemental table 3 shows Dice scores with THOMAS for the rsfMRI parcellations, with and without regrouping, again showing the potential ability of rsfMRI to subdivide larger structural nuclei like Pul and Md into subnuclei.

The DTI-based method parcellates the thalamus into seven regions. This choice seems arbitrary although this parameter has been used in previous DTI studies [such as Behrens (2003)] in correspondence with the number of presegmented cortical targets and has also been shown to yield the most consistent parcellation (Battistella et al. 2017). Supplemental figure 2 shows maximum probability maps for an alternative DTI parcellation using 11 clusters (chosen as to match the number of clusters used by structural parcellation) compared against the seven-cluster parcellation. The alternative parcellation is less stable as evidenced by the decreased contiguity of the map labels. In DTI-based parcellation, the number of clusters generated is an empirically chosen parameter and possibly a source of error, unlike tractography-based parcellation where the number of clusters is determined by cortical targets. Furthermore, the clusters generated by the DTI-based method seem to be rather uniform in size (Supplemental Table 1b) compared to the wide range of volumes generated by THOMAS (Supplemental Table 1a). This is consistent with the ability of DTI to only resolve larger nuclei and one of the seven clusters it produces is a conglomerate, not corresponding to any anatomic nuclei (Battistella et al. 2017).

Relative strengths and weaknesses of the three methods

THOMAS uses a nonstandard pulse sequence (WMn MP-RAGE), while DTI and rsfMRI are acquired more routinely in clinical protocols. The latter two could be viable alternatives for identifying larger nuclei such as the VLp, critical in Deep Brain Stimulation targeting. However, the lower resolution ($2\times2\times3$ mm for DTI, 2.5 mm isotropic for rsfMRI) of these image types limits their ability to independently distinguish smaller nuclei, some of which are only a few voxels in extent. Furthermore, DTI- and rsfMRI-based methods generate unlabeled clusters which are identified and labeled relative to the THOMAS clusters, reducing the independence of those pipelines. Higher resolution DTI and fMRI could enhance the accuracy of these parcellations. The use of techniques such as MUSE (Chen et al. 2013) can enable higher resolution (sub mm) DTI and rsfMRI via multi-shot EPI. Alternatively, superresolution techniques have been developed to synthesize high-resolution DTI using multiple low-resolution images (Peled and Yeshurun 2001) but are susceptible to subject motion.

Local DTI parcellation is advantageous relative to global methods in that long-distance fiber tracking may be unreliable in patients with pathology such tumors or white matter or gray matter lesions, which will disrupt the tractography process. However, exclusive reliance upon local diffusion behavior in analyzing thalamic substructure may also be of limited utility. The thalamus is a predominantly gray matter structure with low fractional anisotropy, and so the degree to which the complex FODs used by this method are representative of true architecture is questionable. Additional examination would be warranted to explore the effect of varying DTI acquisition parameters upon the final parcellation product. A technique leveraging properties of multiple shell collections (Multi-shell, multi-tissue constrained spherical deconvolution, or MSMT CSD) has been developed that allows for the estimation and isolation of WM-only FODs; parcellation based upon these may be more reflective of relevant myelinated structure. Of course, the predominance of gray matter in the thalamus could call into question the utility of WM-only FODs. Collecting a larger number of diffusion directions during DTI acquisition (and using higher *b*-values) would permit the use of higher order spherical harmonic basis functions in FOD modeling schema, which in turn could allow for improved identification of smaller scale structures in the parcellation process.

Limitations of our work

Our test data set was limited to a set of eighteen healthy subjects. More work would be needed to validate the correspondence of the three methods in the presence of pathology. In the absence of manual parcellation ground truth, THOMAS was used as a proxy. It had the highest spatial resolution of the three acquisition techniques and has been thoroughly validated against manual parcellation guided by the Morel atlas on control subjects and patients with multiple sclerosis. It has also been clinically validated in multiple sclerosis (Planche et al. 2019) and in alcohol use disorder (Zahr et al. 2019). In addition, the use of multi-atlas segmentation makes it more robust than single-atlas-based methods (Rohlfing et al. 2003) such as the Krauth atlas (which is an average of the five subjects in the Morel atlas in MNI space) (Krauth et al. 2010). As previously mentioned, THOMAS does not subdivide the mediodorsal or pulvinar nucleus into subnuclei as in the Morel atlas. This may be the reason for lower Dice scores between THOMAS and rsfMRI parcellation for those nuclei. In general, the differing numbers of clusters between methods complicate comparisons, but these parameters were chosen in part to optimize stability and consistency across subjects. For comparison purposes, we have

reported results of using 11 clusters for all methods in the Supplemental section.

Future work

The maps in Supplemental Fig. 1 suggest that rsfMRI parcellation may consistently identify subdivisions of larger structural nuclei (particularly the Md and Pul). A hierarchical fusion of structural and functional parcellations would be valuable when routine rsfMRI spatial resolution becomes comparable to that of structural imaging, which is possible at the moment only on 7 T using specialized hardware. A one-to-one mapping of structure and function might be needed to sensibly merge data from functional and structural imaging which could be informed by animal models where such studies are more feasible due to the possibility of histological correlations. Susceptibility weighted images acquired at 7 T have been shown promise as a means of providing supplementary information about the thalamus for DTI collected on the same individual (Abosch et al. 2010). Deep learning could be used to exploit latent relationships between different acquisition modes to produce enhanced parcellation. A multimodal, deep learning-based technique has been developed for the purposes of cortical parcellation (Glasser et al. 2016). This sort of architecture could be trained to leverage relationships between structural, structural connectivity, and functional connectivity localized to the thalamic nuclei.

Conclusion

We have implemented a systematic comparison of structural-, DTI-, and rsfMRI-based thalamus parcellation techniques on a single set of subjects. Each method exhibited strengths and weaknesses that could inform their future use. DTI parcellation corresponds more strongly with structural parcellation in the larger nuclei, while rsfMRI parcellation exhibits closer correspondence with structural parcellation in the smaller nuclei. Increases in the spatial resolution of images used by DTI and rsfMRI parcellation methods would be required to match the performance of structural parcellation in identifying the smaller nuclei.

References

Abosch A, Yacoub E, Ugurbil K, Harel N (2010) An assessment of current brain targets for deep brain stimulation surgery with susceptibilityweightedimaging at 7 tesla. Neurosurgery 67(6):1745–1756

Aggleton J, Brown MW (1999) Episodic memory, amnesia, and the hippocampal–anterior thalamic axis. Behav Brain Sci 22(3):425–444

Andreasen N (1997) The role of the thalamus in schizophrenia. Can J Psychiatry 42(1):27–33. https://doi.org/10.1177/070674379704200104

"ANTs by Stnava". n.d. https://stnava.github.io/ANTs/. Accessed 31 Mar 2019

Barth M et al (2016) Simultaneous multislice (SMS) imaging techniques. Magn Reson Med 75(1):63–81

Basser PJ, Mattiello J, LeBihan D (1994) MR diffusion tensor spectroscopy and imaging. Biophys J 66(1):259–267. https://doi.org/10.1016/S0006-3495(94)80775-1

Basser PJ et al (2000) In Vivo fiber tractography using DT-MRI data. Magn Reson Med 44(4):625–632. https://doi.org/10.1002/1522-2594(200010)44:4%3c625:AID-MRM17%3e3.0.CO;2-O

Battistella G et al (2017) Robust thalamic nuclei segmentation method based on local diffusion magnetic resonance properties. Brain Struct Funct 222(5):2203–2216. https://doi.org/10.1007/s00429-016-1336-4

Beckmann CF, Smith SM (2004) Probabilistic independent component analysis for functional magnetic resonance imaging. IEEE Trans Med Imaging 23(2):137–152. https://doi.org/10.1109/TMI.2003.822821

Beckmann CF, Mackay CE, Filippini N, Smith SM (2009) Group comparison of resting- state FMRI data using multi-subject ICA and dual regression. Neuroimage 47(Suppl 1):S148

Behrens TEJ et al (2003) Non-invasive mapping of connections between human thalamus and cortex using diffusion imaging. Nat Neurosci 6(7):750–757. https://doi.org/10.1038/nn1075

Benabid AL et al (1991) Long-term suppression of tremor by chronic stimulation of the ventral intermediate thalamic nucleus. Lancet 337(8738):403–406. https://doi.org/10.1016/0140-6736(91)91175-T

Braak H, Braak E (1991) Alzheimer's disease affects limbic nuclei of the thalamus. Acta Neuropathol 81(3):261–268

Byne W et al (2001) Magnetic resonance imaging of the thalamic mediodorsal nucleus and pulvinar in schizophrenia and schizotypal personality disorder. Arch Gen Psychiatry 58(2):133–140

Chen W et al (1998) Human primary visual cortex and lateral geniculate nucleus activation during visual imagery. NeuroReport 9(16):3669–3674

Chen NK et al (2013) A robust multi-shot scan strategy for high-resolution diffusion weighted MRI enabled by multiplexed sensitivity-encoding (MUSE). NeuroImage 72(May):41–47. https://doi.org/10.1016/j.neuroimage.2013.01.038

Deoni SCL et al (2005) Visualization of thalamic nuclei on high resolution, multi-averaged T1 and T2 maps acquired at 1.5 T. Hum Brain Mapp 25(3):353–359. https://doi.org/10.1002/hbm.20117

"Generalized Autocalibrating Partially Parallel Acquisitions (GRAPPA)-Griswold (2002) Magnetic Resonance in Medicine, Wiley Online Library". n.d. https://onlinelibrary.wiley.com/doi/full/10.1002/mrm.10171. Accessed 6 June 2019

Glasser MF et al (2016) A multi-modal parcellation of human cerebral cortex. Nature 536(7615):171

Henderson JM, Carpenter K, Cartwright H, Halliday GM (2000) Loss of thalamic intralaminar nuclei in progressive supranuclear palsy and Parkinson's disease: clinical and therapeutic implications. Brain 123(7):1410–1421. https://doi.org/10.1093/brain/123.7.1410

Iglesias JE et al (2018) A probabilistic atlas of the human thalamic nuclei combining ex vivo MRI and histology. Neuroimage 183:314–326

Jbabdi S, Woolrich MW, Behrens TEJ (2009) Multiple-subjects connectivity-based parcellation using hierarchical dirichlet process mixture models. NeuroImage 44(2):373–384. https://doi.org/10.1016/j.neuroimage.2008.08.044

Jenkinson M, Smith S (2001) A global optimisation method for robust affine registration of brain images. Med Image Anal 5(2):143–156. https://doi.org/10.1016/S1361-8415(01)00036-6

Ji B et al (2016) Dynamic thalamus parcellation from resting-state fMRI data. Hum Brain Mapp 37(3):954–967

Krauth A et al (2010) A mean three-dimensional atlas of the human thalamus: generation from multiple histological data. Neuroimage 49(3):2053–2062

Kumar VJ, Mang S, Grodd W (2015) Direct diffusion-based parcellation of the human thalamus. Brain Struct Funct 220(3):1619–1635. https://doi.org/10.1007/s00429-014-0748-2

Kumar VJ et al (2017) Functional anatomy of the human thalamus at rest. NeuroImage 147(February):678–691. https://doi.org/10.1016/j.neuroimage.2016.12.071

Lee HL et al (2013) Tracking dynamic resting-state networks at higher frequencies using MR-encephalography. NeuroImage 65:216–222. https://doi.org/10.1016/j.neuroimage.2012.10.015

Mang SC et al (2012) Thalamus segmentation based on the local diffusion direction: a group study. Magn Reson Med 67(1):118–126. https://doi.org/10.1002/mrm.22996

Morel A, Magnin M, Jeanmonod D (1997) Multiarchitectonic and stereotactic atlas of the human thalamus. J Comp Neurol 387(4):588–630. https://doi.org/10.1002/(SICI)1096-9861(19971103)387:4%3c588:AID-CNE8%3e3.0.CO;2-Z

Muschelli J et al (2014) Reduction of motion-related artifacts in resting state FMRI using ACompCor. NeuroImage 96:22–35. https://doi.org/10.1016/j.neuroimage.2014.03.028

Najdenovska E et al (2018) In-vivo probabilistic atlas of human thalamic nuclei based on diffusion-weighted magnetic resonance imaging. Sci Data 5:180270. https://doi.org/10.1038/sdata.2018.270

Nickerson LD, Smith SM, Öngür D, Beckmann CF (2017) Using dual regression to investigate network shape and amplitude in functional connectivity analyses. Front Neurosci. https://doi.org/10.3389/fnins.2017.00115

O'Mara SM (2013) The anterior thalamus provides a subcortical circuit supporting memory and spatial navigation. Front System Neurosci 7(45)

O'Muircheartaigh J, Vollmar C, Traynor C, Barker GJ, Kumari V, Symms MR, Thompson P, Duncan JS, Koepp MJ, Richardson MP (2011) Clustering probabilistic tractograms using independent component analysis applied to the thalamus. Neuroimage 54(3):2020–2032

van Oort ESB et al (2018) Functional parcellation using time courses of instantaneous connectivity. NeuroImage Segm Brain 170:31–40. https://doi.org/10.1016/j.neuroimage.2017.07.027

Patenaude B, Smith SM, Kennedy DN, Jenkinson M (2011) A bayesian model of shape and appearance for subcortical brain segmentation. NeuroImage 56(3):907–922. https://doi.org/10.1016/j.neuroimage.2011.02.046

Planche V et al (2019) White-matter-nulled MPRAGE at 7T reveals thalamic lesions and atrophy of specific thalamic nuclei in multiple sclerosis. Mult Scler J p. 1352458519828297

Peled S, Yeshurun Y (2001) Superresolution in MRI: application to human white matter fiber tract visualization by diffusion tensor imaging. Magn Reson Med 45(1):29–35. https://doi.org/10.1002/1522-2594(200101)45:1%3c29:AID-MRM1005%3e3.0.CO;2-Z

Rittner L, Lotufo RA, Campbell J, Pike GB (2010) Segmentation of thalamic nuclei based on tensorial morphological gradient of diffusion tensor fields. IEEE Int Symp Biomed Imaging Nano Macro. https://doi.org/10.1109/ISBI.2010.5490203

Rohlfing T, Russakoff DB, Maurer CR (2003) An expectation maximization-like algorithm for multi-atlas multi-label segmentation. In: Bildverarbeitung für die Medizin Springer, Berlin, Heidelberg, pp 348–352

Saranathan M et al (2015) Optimization of white-matter-nulled magnetization prepared rapid gradient echo (MP-RAGE) imaging. Magn Reson Med 73(5):1786–1794. https://doi.org/10.1002/mrm.25298

Satterthwaite TD et al (2013) An improved framework for confound regression and filtering for control of motion artifact in the preprocessing of resting-state functional connectivity data. NeuroImage 64:240–256. https://doi.org/10.1016/j.neuroimage.2012.08.052

Schiff ND (2010) Recovery of consciousness after brain injury: a mesocircuit hypothesis. Trends Neurosci 33(1):1–9

Schiff ND et al (2007) Behavioural improvements with thalamic stimulation after severe traumatic brain injury. Nature 448(7153):600

Schmitt LI et al (2017) Thalamic amplification of cortical connectivity sustains attentional control. Nature 545(7653):219

"Simultaneous Multislice (SMS) Imaging Techniques-Barth (2016) Magnetic Resonance in Medicine, Wiley Online Library" n.d. https://onlinelibrary.wiley.com/doi/full/10.1002/mrm.25897. Accessed 6 June 2019

Smith SM et al (2004) Advances in functional and structural MR image analysis and implementation as FSL. NeuroImage Math Brain Imaging 23(January):S208–S219. https://doi.org/10.1016/j.neuroimage.2004.07.051

Su JH et al (2019) Fast, fully automated segmentation of thalamic nuclei from structural MRI. NeuroImage. https://doi.org/10.1016/j.neuroimage.2019.03.021

Sudhyadhom A, Haq IU, Foote KD, Okun MS, Bova FJ (2009) A high resolution and high contrast MRI for differentiation of subcortical structures for DBS targeting: the fast gray matter acquisition T1 inversion recovery (FGATIR). Neuroimage 47:T44–T52

Tourdias T, Saranathan M, Levesque IR, Su J, Rutt BK (2014) Visualization of intra-thalamic nuclei with optimized white-matter-nulled MP-RAGE at 7T. NeuroImage 84:534–545. https://doi.org/10.1016/j.neuroimage.2013.08.069

Traynor CR et al (2011) Segmentation of the thalamus in MRI Based on T1 and T2. NeuroImage 56(3):939–950. https://doi.org/10.1016/j.neuroimage.2011.01.083

Tuch DS (2004) Q-Ball Imaging. Magn Reson Med 52(6):1358–1372. https://doi.org/10.1002/mrm.20279

Unrath A et al (2008) Directional colour encoding of the human thalamus by diffusion tensor imaging. Neurosci Lett 434(3):322–327. https://doi.org/10.1016/j.neulet.2008.02.013

Wang H, Yushkevich P (2013) Multi-atlas segmentation with joint label fusion and corrective learning: an open source implementation. Front Neuroinform. https://doi.org/10.3389/fninf.2013.00027

Watanabe Y, Funahashi S (2012) Thalamic mediodorsal nucleus and working memory. Neurosci Biobehav Rev 36(1):134–142

Wiegell MR, Tuch DS, Larsson HBW, Wedeen VJ (2003) Automatic segmentation of thalamic nuclei from diffusion tensor magnetic resonance imaging. NeuroImage 19(2):391–401. https://doi.org/10.1016/S1053-8119(03)00044-2

Wimmer RD et al (2015) Thalamic control of sensory selection in divided attention. Nature 526(7575):705

Wu CW et al (2008) Frequency specificity of functional connectivity in brain networks. NeuroImage 42(3):1047–1055. https://doi.org/10.1016/j.neuroimage.2008.05.035

Yamada K, Akazawa K, Yuen S, Goto M, Matsushima S, Takahata A, Nakagawa M, Mineura K, Nishimura T (2010) MR imaging of ventral thalamic nuclei. Am J Neuroradiol 31(4):732–735. https://doi.org/10.3174/ajnr.A1870

Zahr NM, Sullivan EV, Pohl KM, Pfefferbaum A, Saranathan M (2020) Sensitivity of ventrolateral posterior thalamic nucleus to back pain in alcoholism and CD4 nadir in HIV. Human Brain Mapping 41(5):1351–1361

Zhang D, Snyder AZ, Fox MD, Sansbury MW, Shimony JS, Raichle ME (2008) Intrinsic functional relations between human cerebral cortexand thalamus. J neurophysiol 100(4):1740–1748